Journal of The Electrochemical Society

OPEN ACCESS

On the Correlation between the Oxygen in Hydrogen Content and the Catalytic Activity of Cathode Catalysts in PEM Water Electrolysis

To cite this article: Agate Martin *et al* 2021 *J. Electrochem. Soc.* **168** 114513

Journal of The Electrochemical Society, 2021 **168** 114513

On the Correlation between the Oxygen in Hydrogen Content and the Catalytic Activity of Cathode Catalysts in PEM Water Electrolysis

Agate Martin,[1] Patrick Trinke,[1] Chuyen Van Pham,[2] Melanie Bühler,[3,4] Markus Bierling,[2,5] Peter K. R. Holzapfel,[2,6] Boris Bensmann,[1,z] Simon Thiele,[2,5] and Richard Hanke-Rauschenbach[1]

[1]*Leibniz University Hannover, Institute of Electric Power Systems, 30167 Hannover, Germany*
[2]*Forschungszentrum Jülich GmbH, Helmholtz Institute Erlangen-Nürnberg for Renewable Energy (IEK-11), 91058 Erlangen, Germany*
[3]*Electrochemical Energy Systems, Department of Microsystems Engineering, Albert-Ludwigs-University of Freiburg, 79110 Freiburg, Germany*
[4]*Hahn-Schickard, 79110 Freiburg, Germany*
[5]*Department of Chemical and Biological Engineering, Friedrich-Alexander-Universität Erlangen-Nürnberg, 91058 Erlangen, Germany*
[6]*Technical University of Berlin, Chair of Sustainable Engineering, 10623 Berlin, Germany*

Altogether five platinum group metal (PGM) and PGM-free cathode catalysts were investigated in full PEM water electrolysis cells regarding their polarisation behaviour and their hydrogen and oxygen recombination properties. It was shown that the recombination activity of permeated oxygen and evolved hydrogen within the cathodic catalyst layer correlates with the activity of the oxygen reduction reaction (ORR) which was determined *ex situ* with linear sweep voltammetry. We found that the investigated PGM-free cathode catalysts had a low activity for the ORR resulting in higher measurable oxygen in hydrogen volume fractions compared to the PGM catalysts, which are more active for the ORR. Out of the three investigated PGM-free catalysts, only one commercially available material based on a Ti suboxide showed a similar good polarisation behaviour as the state of the art cathode catalyst platinum, while its recombination activity was the lowest of all catalysts. In addition to the recombination of hydrogen and oxygen on the electrocatalysts, we found that the prevalent carbon-based cathodic porous transport layers (PTL) also offer catalytically active recombination sites. In comparison to an inactive PTL, the measurable oxygen flux using carbon-based PTLs was lower and the recombination was enhanced by microporous coatings with high surface areas.
 [DOI: 10.1149/1945-7111/ac38f6]

Manuscript submitted April 16, 2021; revised manuscript received October 28, 2021. Published November 22, 2021.

Supplementary material for this article is available online

Hydrogen has a central role in future energy storage scenarios. Polymer electrolyte membrane water electrolysers (PEMWE) are expected to account for a significant share of the hydrogen production facilities in order to fulfil the raising demand.[1,2] However, if significant upscaling of the technology is demanded, two important aspects related to the cathode catalyst material have to be investigated in more detail. Firstly, only the usage of precious platinum group metals (PGM) as electrocatalysts allow a good electrochemical polarisation behaviour and therefore minimal operating costs.[3,4] Secondly, hydrogen purity and the cell's lifetime strongly correlate with oxygen permeation across the cell.[5] As the state of the art materials platinum and iridium may get more expensive due to their scarcity, alternative catalyst designs and materials are required, if the demand raises.[1,2,6] A key challenge within the research field is to find more abundant catalyst materials which withstand the harsh electrochemical environment caused by the low pH of the acidic membrane and the prevailing electric potentials at the electrodes.[1,7–10]

In order to compete with platinum as a hydrogen evolving catalyst, the reaction kinetics has to be as fast as possible so that the cathodic kinetic losses on the cell voltage are kept at a minimum. Another aspect for further investigations are possible side reactions caused by gas crossover.

Also, from PEM fuel cells it is known that the permeation of hydrogen gas from the anode to the cathode leads to the formation of reactive oxygen species, such as hydroxyl radicals, on the platinum particles.[11–13] In PEM water electrolysis, similar problems occur. The crossover of evolved hydrogen to the anode reduces the efficiency and may form an explosive gas mixture.[14] The same applies to the crossover of evolved oxygen to the cathode. In this case, however, the recombination of both gases to water consumes even more hydrogen and the mentioned radicals are formed by either a chemical or electrochemical pathway.[15] The reactivity of these intermediates is high enough to attack the polymeric backbone of the membrane leading to performance losses due to material degradation and eventually to cell failure and a shortened lifetime.[10–13,16–18] Thus, a deeper understanding on oxygen permeation is crucial. Extensive experimental and theoretical studies on hydrogen crossover were performed in our research group[5,19,20] and by others.[21,22]

As the formation of the intermediate radicals is catalysed by platinum and other impurities such as Fe-ions,[12,15,16] the research on finding new cathode catalysts may also lead to an enhancement of the lifetime, as radical formation might be suppressed. However, less recombination of oxygen and hydrogen at the cathode catalyst reduces the purity of the produced hydrogen. The subsequent purification of the gas is necessary for the most potential hydrogen applications such as fuel cells, which leads to further costs. Besides this extra effort, the system safety is not guaranteed if the oxygen in hydrogen volume exceeds the lower explosion limit (approximately 5% O_2 in H_2[14]). Recently, Trinke *et al.*[23] evidenced the increase in oxygen crossover with increasing current density in PEM electrolysis using platinum and a platinum-free (Pt-free) cathode catalyst. The investigations showed an increased oxygen in hydrogen fraction when using the Pt-free catalyst, which is ascribed to the lower recombination activity compared to platinum. Hence, the evaluation of cathode catalysts is possible by measuring their polarisation behaviour regarding the hydrogen evolution reaction (HER) and their recombination properties, by means of their activity towards

[z]E-mail: boris.bensmann@ifes.uni-hannover.de

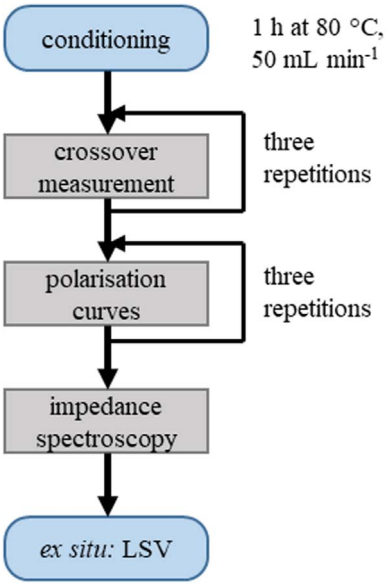

Figure 1. Illustration of the used electrochemical measurement sequence.

the oxygen reduction reaction (ORR) and the measurable oxygen in hydrogen content.

In this study, we investigated the polarisation behaviour of PEM electrolysis cells using five different cathode catalysts. Pt/C is used as a benchmark catalyst within this study, as it is the state of the art cathode catalyst for the HER. As another PGM catalyst, IrO_2 is used. IrO_2 is reported to be a very good hydrogen evolving electrocatalyst.[24–26] Moreover, three different PGM-free catalysts were investigated. The first one is based on a commercially available PGM-free cathode catalyst for PEM electrolysis. The catalyst (named "Magnéli phase" in this work) is a modified version of Ebonex® which consists of titanium suboxides in Magnéli phase.[27] The other two catalysts are completely PGM-free and are based on nitrogen doped carbon nanotubes (N-doped CNT). Recently, Zeng *et al.*[28] reported that N-doped CNTs are promising electrocatalysts for the HER and the ORR. Hinnemann *et al.*[8] identified molybdenum sulfides as a possible candidate for the HER via computational simulations. Other research groups confirmed the materials catalytic activity experimentally.[6,7,9,29–31] However, they also identified that the catalyst design is very important as only the particle edges are active for HER. As the bulk material is a rather bad electronic conductor, it needs a suitable substrate such as the aforementioned N-doped CNT. In a recent work, Holzapfel *et al.*[32] introduced $[Mo_3S_{13}]^{2-}$@N-doped CNT as a cathode catalyst in full PEM electrolysis cells and report current densities of almost 4 A cm^{-2} at a cell voltage of 2.3 V when using a Nafion 212 membrane. We extended the ordinary electrochemical characterisation (polarisation curves, electrochemical impedance spectroscopy and linear sweep voltammetry) by measuring the permeated oxygen in the cathodic product gas to draw conclusions on the recombination characteristics of the used catalysts.

Experimental

Setup and materials.—In this study, commercial Nafion 115 membranes with only an anodic catalyst layer consisting of iridium (2.0 mg cm^{-2} Ir-black, Hiat gGmbH) and an active area of 25 cm^2 were used. The anodic porous transport layer (PTL) was a titanium fibre (1 mm, titanium grade 1, 2GDL40–1.00, Bekaert).

For the cathode side, porous transport electrodes (PTE), based on carbon PTLs with a microporous layer (MPL) (H24C5, Freudenberg SE) were used as a substrate for the following catalysts: Pt/C (0.5 mg cm^{-2}, HiSPEC 9100, Alfa Aesar), IrO_2 (1.5 mg cm^{-2}, Premion, Alfa Aesar), Magnéli phase catalyst (1.5 mg cm^{-2}, Pt-free, Hiat gGmbH), N-doped CNT (1.5 mg cm^{-2}, ACS Material) and $[Mo_3S_{13}]^{2-}$@N-doped CNT (1.5 mg cm^{-2}, self-synthesized according to Holzapfel *et al.*[32]).

The catalyst layers were deposited onto the substrates by spray coating (Exacta Coat, Sono-Tek). The height of the ultrasonic nozzle was set to 37 mm, the shaping air pressure was 0.6 kPa, speed 170 mm s^{-1}, flow rate 0.5 ml min^{-1} and the ultrasonication energy was set to 5 W at 48 kHz. The PTLs were fixed on a hot plate set to 110 °C. The coating inks consisted of 1 wt% solids (catalyst powder and Nafion D520, FuelCellStore) in a mixture of deionised water and 2-propanol as solvents. The ratio of water and 2-propanol was 1:1 for $[Mo_3S_{13}]^{2-}$@N-CNT mixed with 10 wt% carbon black (Vulcan XC-72R, FuelCellsEtc). For Pt/C and the Magnéli phase catalyst a ratio of 1:3 was chosen for better ink stability. The ionomer content was 20 wt% of the solid part. The ink mixing was performed as described elsewhere[33] with the difference of stirring for two days in between the sonication steps.

Before cell assembly, the Ti-PTL was sonicated for 15 min in deionised water to remove contaminants and the half-coated membrane was immersed into deionised water for about an hour. Then, the Ti-PTL, the wet half-coated membrane and the PTE were assembled. The membrane electrode assemblies (MEAs) were analysed in a quickCONNECTfixture qCf FC25/100 (LC) frame and a 5 × 5 cm^2 electrolyser cell (baltic FuelCells GmbH). The pressure on the active area is controlled by a pneumatic actuator in the cell and was set to 4.5 bar(g), which corresponds to an approximate clamping pressure of 1.4 MPa.[34] The cell has parallel flow fields with 1.87 mm wide lands and 2.5 mm wide channels on both electrodes. For maintaining a constant cell temperature of 80 °C, the cell was tempered with a circulation thermostat (ministat 230, Huber AG). The cell temperature was monitored by thermal sensors placed closely to the flow fields.

The crossover measurements and electrochemical characterisation were performed at ambient pressure in a teststation (E100, Greenlight Innovation) at 80 °C with deionised water supply of 50 ml min^{-1} on the anode side only.

Data acquisition.—For the structural analysis, small parts of the PTEs were fixed on an aluminium SEM specimen stub with conductive carbon pads. The samples were coated with gold (108 Manual Sputter Coater, Cressington) to increase the electric conductivity of the samples. Imaging was done with a focused ion beam scanning electron microscope (FIB-SEM, Crossbeam 540, Zeiss) with a Gemini II column. Surface images were obtained by applying an acceleration voltage of 3 kV and a beam current of 750 pA. Additionally, cross-sectional images of all five samples were taken. For this, a protective platinum layer was deposited on all samples (except the N-doped CNT) via ion beam deposition using a gas injection system (Orsay Physics, MonoGIS). The trenches were cut with a 30 kV and 7 nA ion beam. The cross-sections were polished in two steps (first with 1.30 kV and 700 pA and then with 2.30 kV and 100 pA). Finally, the cross-sectional SEM images were obtained by applying an acceleration voltage of 3 kV and a beam current of 750 pA.

The order of the electrochemical measurements is illustrated in Fig. 1. Prior to the electrochemical testing, the cells were tempered at 80 °C with deionised water with a supply of 50 ml min^{-1} on the anode side only. The measurement protocol started with three subsequent measurements of the gas crossover from 0.1 A cm^{-2} up to 2 A cm^{-2}. Each current density step was held until a steady state in the gas mixtures was reached. Only the third data set was used for further analysis, as they were the most stable.

After the crossover measurements, three subsequent polarisation curves were recorded. Only the third data set was used for further analysis as no divergences between the curves were observed. Then, electrochemical impedance spectra were recorded. The catalysts were scraped off the analysed PTEs in order to measure their catalytic activities *ex situ* with linear sweep voltammetry (LSV).

Crossover measurements.—For the gas crossover measurement, the cells were operated galvanostatically with a DC current supply (XG 6–220, Sorensen) from 0.1 A cm^{-2} to 2 A cm^{-2}. The holding time at the investigated current densities was adjusted to the different production rates until a steady state in the measured gas composition was reached. As the gas production rates are low at low current densities, the holding times were longer. For the investigated current densities (0.1, 0.2, 0.4, 0.6, 1, 1.5 and 2 A cm^{-2}), the holding times were set to 7, 5, 3, 2.5, 2, 1.5 and 1 h, respectively. The cathodic product gas was analysed with a gas chromatograph (490 Micro GC System, Agilent). Helium was used as a carrier gas. The gas samples were separated in 5 Å mole sieve columns of 10 m length and were analysed with an integrated thermal conductivity detector. Prior to analysis of the dried cathode product gas, the chromatograph was calibrated with O_2 in H_2 mixtures in known concentrations.

Polarisation curves.—The polarisation curves were recorded from 0.01 A cm^{-2} to 2 A cm^{-2} with a Solartron ModuLab XM PSTAT with a power booster (6 V/100 A) in logarithmic decimal current density steps. The holding time was approximately 25 s and included the measurement of the high frequency resistance R_{HF} from 10 kHz to 100 Hz with a 10% root mean square (RMS).

Electrochemical impedance spectroscopy.—Full electrochemical impedance spectra at 0.1, 0.5, 1.0, 1.5 and 2.0 A cm^{-2} were recorded in a frequency range of 100 kHz to 100 mHz with 7 points per decade and a 10% RMS using the same hardware as for recording the polarisation curves.

Data evaluation.— *Polarisation curves.*—For an analysis of the cell kinetics, the measured polarisation curves were corrected by the ohmic potential drop (Eq. 1).

$$U_{iR_{HF}-free} = U_{cell} - i \cdot R_{HF} \quad [1]$$

It is assumed that the ohmic cell resistance is equal to the measured high frequency impedance R_{HF} where the imaginary part of the impedance equals zero. These high frequency resistances were obtained by interpolating the respective Nyquist plots at the intercept with the real axis linearly.

For a further analysis of the iR_{HF}-free cell voltage, the standard cell potential at 80 °C (U°_{cell} = 1.18 V) was subtracted to obtain the remaining overpotentials η (Eq. 2).

$$\eta = U_{iR_{HF}\text{-free}} - U^{\circ}_{cell} \quad [2]$$

Quantification of oxygen permeation and oxygen content.—The oxygen volume fraction in cathode product gas $\varphi^{c,out}_{O_2}$ can be expressed by Eq. 3.

$$\varphi^{c,out}_{O_2} = \frac{N^{c,out}_{O_2}}{N^{evolved}_{H_2} - N^{perm}_{H_2} + N^{c,out}_{O_2}} \approx \frac{N^{c,out}_{O_2}}{N^{evolved}_{H_2}} \quad [3]$$

$N^{c,out}_{O_2}$ is the oxygen flux in the dried cathode product gas, $N^{evolved}_{H_2}$ is the amount of evolved hydrogen and $N^{perm}_{H_2}$ equals to the permeated hydrogen to the anode. As the amount of $N^{perm}_{H_2}$ and $N^{c,out}_{O_2}$ are very small compared to the amount of evolved hydrogen, the values can be neglected in the denominator for calculation (errors up to ≈ 2%). Then, $N^{c,out}_{O_2}$ can be expressed by Eq. 4.

$$N^{c,out}_{O_2} \approx \varphi^{c,out}_{O_2} \cdot N^{evolved}_{H_2} = \varphi^{c,out}_{O_2} \cdot \frac{i}{2 \cdot F} \quad [4]$$

The permeation of oxygen from the anode through the membrane into the cathodic compartment is assumed to be a result of diffusive and convective transport mechanisms.[23,35] However, the minimum, theoretical flux of oxygen caused purely by diffusion across a Nafion membrane $N^{diff}_{O_2}$ can be calculated according to Eq. 5.[22,36]

$$N^{diff}_{O_2} = P_{O_2} \cdot \frac{\Delta p_{O_2}}{\delta_{mem}} \quad [5]$$

P_{O_2} is the permeability coefficient of oxygen through a wet Nafion membrane (≈2.52 ·10– 9 mo m^{-1} s^{-1} bar^{-1} at 80 °C[22]) and δ_{mem} is the wet membrane thickness (≈152 µm[22]). The oxygen partial pressure difference is described by Δp_{O_2}. The partial pressure of oxygen at the cathode is assumed to be negligible, whereas the

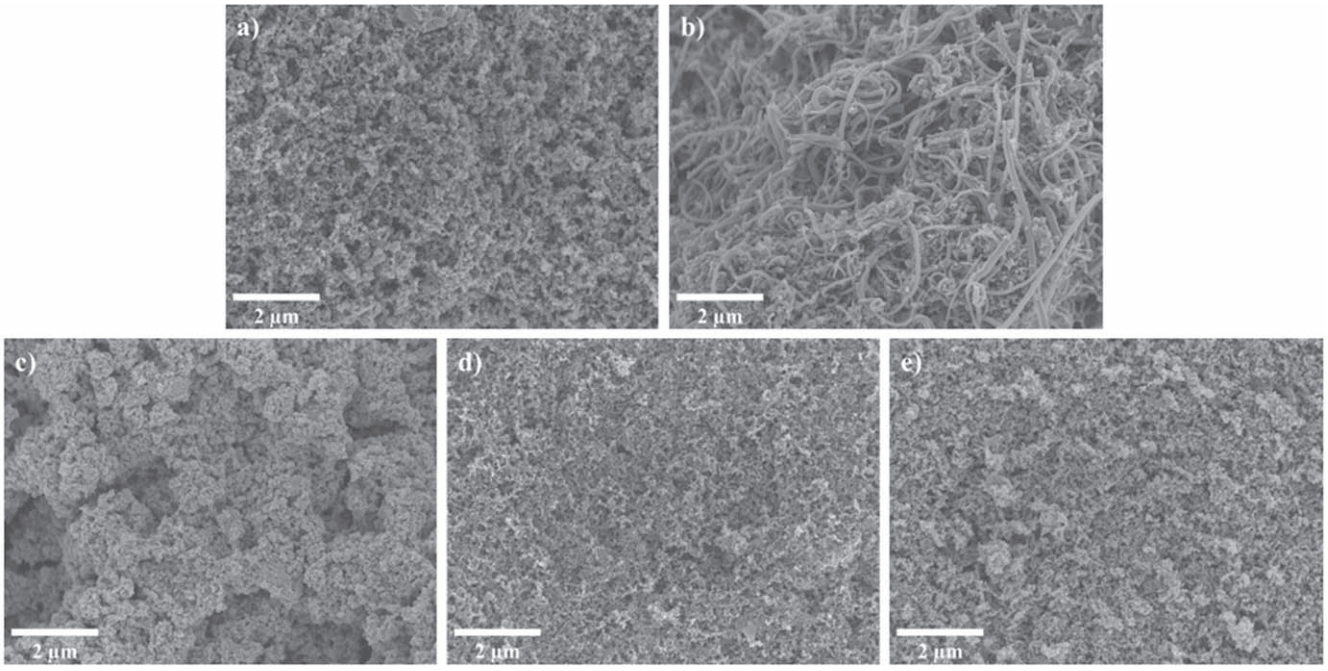

Figure 2. SEM surface images of a) $[Mo_3S_{13}]^{2-}$@N-CNT, b) N-doped CNT, c) IrO_2, d) Magnéli phase and e) Pt/C.

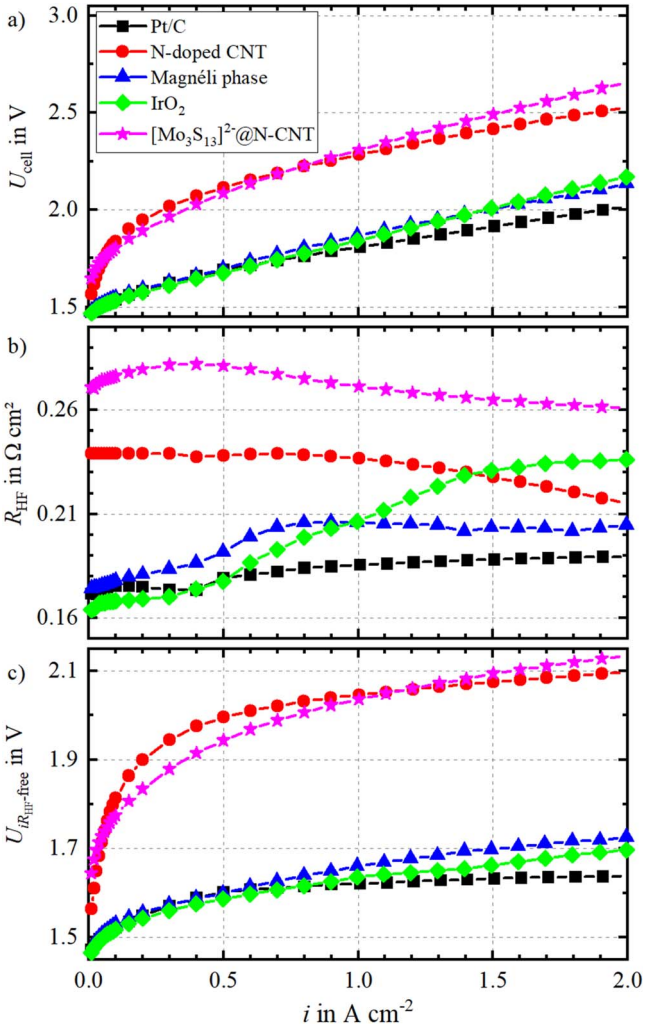

Figure 3. Measured polarisation curves in a), high frequency resistances R_{HF} in b) and iR_{HF}-corrected cell voltages in c) of the five cell configurations, each with another cathode electrocatalyst at 80 °C and ambient pressure.

anodic oxygen partial pressure is equal to the total anodic pressure of 1 bar subtracted by the vapour pressure of water at 80 °C (≈0.4737 bar[37]). For these conditions, an oxygen partial pressure difference of $\Delta p_{O_2} = 0.5263$ bar follows. The diffusional oxygen permeation rate is assumed to be constant over the investigated range of current density, as the pressure and temperature can be assumed as almost constant of the applied current density. This yields a diffusive oxygen permeation of $N_{O_2}^{diff} = 0.0087\ \text{mmol m}^{-2}\ \text{s}^{-1}$.

As explained by Trinke *et al.*,[23] the main reason for the convective oxygen transport could be a result of the electro-osmotic drag of water, which increases with the applied current density.[35] Thus, it can be assumed that the permeation rate of oxygen also shows a current dependency. However, the ratio between the diffusive and convective transport processes cannot be distinguished as it is impossible to measure the convective transport without the diffusive transport as well as an unknown amount of permeated oxygen recombines with hydrogen. Accordingly, we assume that $N_{O_2}^{diff}$ is the minimum oxygen flux within the cathodic compartment, when no convective transport (i.e. at 0 A cm^{-2}) and no recombination takes place.

Results and Discussion

Structural characterisation of the porous transport electrodes.—The surfaces of the PTEs were assessed by scanning electron microscopy (SEM), see Fig. 2. The surfaces imply that the catalyst layer structures are different from one another. The surfaces of the N-CNTs (Fig. 2b) and IrO_2 (Fig. 2c) appear more inhomogeneous than the others. Due to the random positioning of the CNTs, the resulting pore network is inhomogeneous as well. This is also visible in the cross-sectional SEM image of the PTE in Fig. S4 (available online at stacks.iop.org/JES/168/114513/mmedia) within the supplemental information. The CNTs form an inhomogeneous pore network, which is also present when using $[Mo_3S_{13}]^{2-}$@N-CNT. Although its surface appeals a homogeneous structure (Fig. 2a), the cross-section reveals large pore areas and large particle clusters (Fig. S3).

The surface of the PTE with the commercial Magnéli phase catalyst (Fig. 2d) shows a fine particle network, which is also visible in the cross-sectional image (Fig. S1). However, there are also big particles (1–3 μm) present. An energy-dispersive X-ray spectroscopic scan (EDXS) revealed that these clusters consist of titanium and oxygen, which fits to the catalyst description of the manufacturer. To our surprise, the EDXS also revealed the existence of iridium within the catalyst layer. As the iridium containing particle clusters are sparsely distributed and also contain titanium and oxygen, we believe that they are made of a binary transition metal Magnéli phase with Ti and Ir. Despite the existence of iridium, we classify this catalyst as PGM-free, since the electrochemical activity of this material is based on its distinct crystallographic structure (cf. low ORR activity Fig. 9).

The structure of the PTE with Pt/C (Figs. 2e) and S5) prove a homogeneous distribution of the catalyst and a homogeneous pore network. Like the Pt/C and Magnéli phase catalysts, IrO_2 was also obtained commercially. The resulting particle-pore network using IrO_2 is similar to Pt/C (Fig. S2). However, the surface already implies a rougher surface structure of the catalyst layer. Although the thickness of the other catalyst layers was not determined, the cross-sectional image of the IrO_2 PTE shows by far the thinnest catalyst layer (Fig. S2). In this particular cross-section, the thickness is only 2–5 μm.

Polarisation behaviour and kinetics.—The polarisation behaviours of the five investigated cell configurations are shown in Fig. 3a). The five curves can be divided into two groups. The three polarisation curves with the lower cell voltage show a good polarisation behaviour whereas the other two curves with higher cell voltages perform rather poor.

In the group of the well performing cells, the configuration with the state of the art cathode catalyst Pt/C shows the lowest cell voltage over the whole current density range. At low current densities, the polarisation behaviours using IrO_2 and the Magnéli phase at the cathode are very close to Pt/C. With increasing current densities, the cell voltages using these two catalyst are approximately 100 mV higher than with Pt/C. When the current density at 2 V is related to the total catalyst mass, the differences become more apparent. When IrO_2 and the Magnéli phase are used, mass specific currents of 0.46 A mg^{-1} and 0.48 A mg^{-1}, respectively, are obtained. With Pt/C, the highest current (0.87 A mg^{-1}) is achieved at this voltage.

The cells with the two carbon-based cathode catalysts (N-doped CNT and $[Mo_3S_{13}]^{2-}$@N-CNT) have higher cell voltages over the entire current density range than the well performing configurations. Up to approximately 0.8 A cm^{-2}, the cell with $[Mo_3S_{13}]^{2-}$@N-CNT shows lower cell voltages than with N-doped CNT. Above this value and intensifying with increasing current density, the cell with N-doped CNT performs better. This divergence in the polarisation behaviour of the cells can be partly dedicated to increases in R_{HF}, as shown in Fig. 3b). In their work, Holzapfel *et al.*[32] used the same $[Mo_3S_{13}]^{2-}$@N-CNT cathode catalyst in a full PEM cell setup. A similar cell polarisation behaviour was achieved using a Nafion 115 membrane (ca. 2.1 V at 1 A cm^{-2} vs 2.25 V in this work).

The high frequency resistances show a strong current dependency (Fig. 3b). The curves can be grouped similarly to the polarisation curves in Fig. 3a). At current densities close to zero, the high

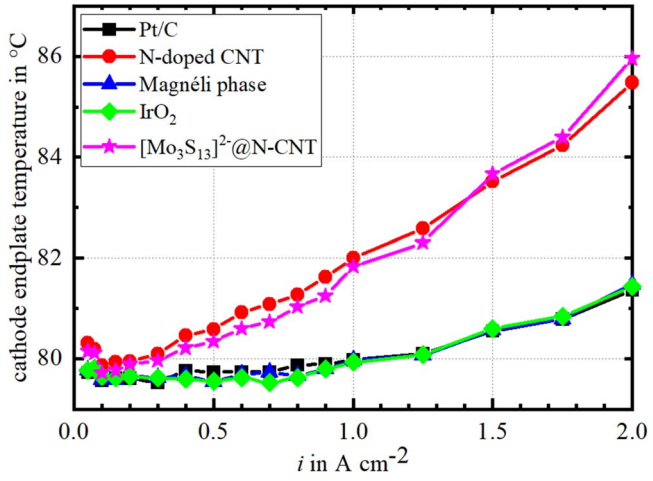

Figure 4. Temperature recorded at the cathodic endplate as a function of the applied current density.

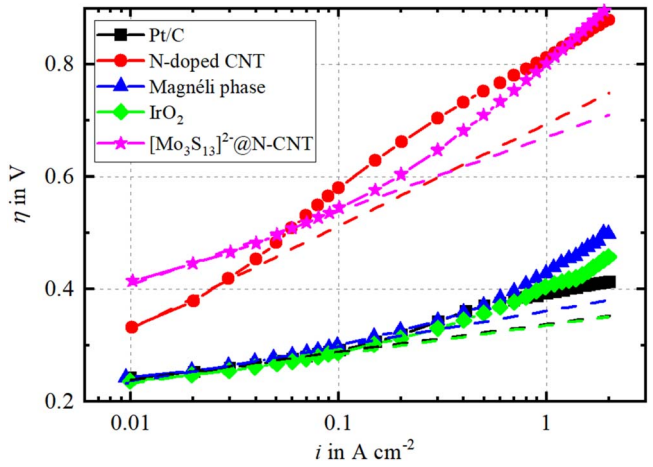

Figure 5. Semi-logarithmic plot of the remaining overpotentials as a function of the current density. The fitted Tafel slopes are extrapolated with dashed lines.

frequency resistances of the good performing catalysts are close to one another. For these three catalysts, R_{HF} increases with increasing current density. However, the absolute increase for Pt/C is very small compared to the other configurations. The increase when using IrO_2 is noticeably steeper and ends at higher R_{HF} values than the N-doped CNT.

The cells using the carbon-based catalysts show significantly higher R_{HF} values compared to the well performing cells. However, the resistances are decreasing with increasing current density. This observation can be explained by the poor polarisation behaviour of these catalysts, which is mainly caused by high overpotentials for the HER. The insufficient cathode kinetics result in more heat production with increasing current density, as shown in Fig. 4. For the two carbon-based catalysts, a temperature increase of approximately 5 K was measured at the cathode endplates, whereas the endplate temperatures of the better performing catalysts remained almost constant over the investigated current range. As the increase in temperature has a positive effect on the ionic conductivity of the membrane, a decrease in R_{HF} can be observed.[38]

Theoretically, the ohmic resistance contains the protonic transport resistance within the membrane, the electric resistance of the PTLs as well as of the metallic bulk material, and interfaces within the cell, and, depending on the location of the reaction zone within the catalyst layer, also protonic and electric losses in the catalyst layer. Normally, the main part of the measured high frequency resistance is related to the protonic losses of the membrane. As the used membrane is identical in all cases, the high frequency resistances should be similar in all cell configurations. For Nafion 115, R_{HF} values between approximately 115 mΩ cm^{-2} [20] and 140 mΩ cm^{-2}[39] were reported. As the measured values in this work (Fig. 3b) lay above the reported values, it can be assumed that more than just the protonic resistances resulting from the membrane were measured. As shown in the previous section, both the surface structure and the catalyst layer structures differ from one another. The catalyst layers with Pt/C, IrO_2 and the Magnéli phase catalyst have a more homogeneous character than the two carbon based catalysts. These differences in structure and the different electronic properties of the catalyst materials also contribute to the measured R_{HF} as stated above. The observed trend in the catalyst layer structures gives hints for possible reasons. As mentioned above, the three well performing catalysts show similar R_{HF} values at low current densities and then increase. The increase for IrO_2 is the highest. The SEM images (cf. surface images in Fig. 2 and cross-sections in Figs. S1 to S5) revealed that this catalyst layer was very thin compared to the others. The different surface structures might have an impact on the resulting contact resistances. The significance of smooth interfaces between the catalyst layer and the membrane for low R_{HF} values was reported previously.[40,41]

A correction of the polarisation curves by iR_{HF} leads to the graphs shown in Fig. 3c). The grouping of the cells remains the same as before. The well performing cathode catalysts are overlapping in the activation regime up to 0.5 A cm^{-2}. From there, the cells containing IrO_2 and the Magnéli phase show additional voltage losses compared to Pt/C. The two curves showing the carbon-based catalysts are barely overlapping in the activation regime and cross each other at 1.2 A cm^{-2}. Since the loading of the state of the art catalyst, Pt/C, is three times lower than that of the other catalysts, the mass specific current was also considered (cf. Fig. S6 in supplemental information). There, the well performing catalysts show the same activation behaviour at small currents. Thus, it can be assumed that the cell kinetics using IrO_2 and the Magnéli phase are still comparable to that of platinum.

The Tafel plot can be obtained from these data when U°_{cell} is subtracted according to Eq. 2 and depicting the abscissa logarithmically. The resulting Fig. 5 contains further indicators for the divergences in the polarisation behaviour, besides increases in R_{HF}. It can be assumed that in the low current density region the overpotentials are dominated by activation processes and that mass transport limitations do not exist until at least a current density of 0.1 A cm^{-2}. One can obtain the Tafel slope by fitting η against the logarithmic current density between 0.01 A cm^{-2} and 0.1 A cm^{-2}. For the N-doped CNTs a fitting interval between 0.01 A cm^{-2} and 0.03 A cm^{-2} was chosen for retaining linearity. From the increasing differences between the extrapolated fits to higher current densities (dashed lines in Fig. 5) and the data sets, other losses such as mass transport resistances and ohmic losses within the catalyst layer can be read.[20,42] In the state of the art cell setup with IrO_2 as anodic catalyst and Pt/C as cathodic catalyst, it is assumed that η_{act} is dominated by the slow oxygen evolution kinetics, whereas the cathodic voltage losses are assumed to be negligible. In this case, the slope in the Tafel representation at low current densities is solely associated to the anode kinetics.

In the present study, this assumption needs to be reassessed. As displayed in Fig. 5, the slopes of the well performing catalysts (Pt/C, IrO_2 and the Magnéli phase) are very close to one another (about 50 to 60 mV dec^{-1}). Assuming that the voltage losses due to the anodic oxygen evolution reaction is the same in all cases and overlap with the hydrogen evolving kinetics, the similar slope indicates similarly fast hydrogen evolution kinetics.

The slopes of the carbon based catalysts are significantly higher compared to the other three catalysts (about 130 mV dec^{-1} for $[Mo_3S_{13}]^{2-}$@N-CNT and 180 mV dec^{-1} for N-doped CNT).

Evidently, the hydrogen evolution kinetics are far slower using these catalysts. In this case, the assumption that the fitted slopes can be assigned completely to the oxygen evolution reaction is not valid anymore. A proper separation of the slope into an anodic and cathodic contribution is not possible as no half-cell potentials were measured.

Further explanations for the different polarisation behaviours of the catalysts can be taken from the electrochemical impedance spectra shown in Fig. 6. The shown impedance spectra were measured at low current densities and represent a kinetically dominated at 100 mA cm^{-2} (Figs. 6a) and 6b) and a resistively dominated region of the cell behaviour at 500 mA cm^{-2} (Figs. 6c) and 6d). The amplitude responses were corrected by R_{HF} in order to allow a more detailed comparison of the catalysts.

The amplitude responses at low frequencies describes the charge transfer resistance R_{CT}. With increasing current density, R_{CT} decreases due to higher reaction rates at the electrodes.[43–45] At both current densities, the amplitude responses of Pt/C, IrO_2 and the Magnéli phase catalyst are almost identical. In comparison, the low frequency amplitude of the carbon-based catalysts ($[Mo_3S_{13}]^{2-}$@N-CNT and N-doped CNT) are higher. At 100 mA cm^{-2}, the amplitude of N-doped CNT is about 1 Ω cm^2 higher than the value for Pt/C whereas the value of $[Mo_3S_{13}]^{2-}$@N-CNT lays in between. At 500 mA cm^{-2}, the low frequency amplitudes of both carbon-based catalysts approach one another. However, the amplitude of the nanotubes at 0.1 Hz is lower than of $[Mo_3S_{13}]^{2-}$@N-CNT.

Similar to the preceding analysis of the Tafel plots (Fig. 5), the integral cell impedance cannot be resolved into an anodic and cathodic contribution. Generally, it is assumed that the sluggish oxygen evolution reaction also dominates the cell impedance.[46–48] As the anodes and the respective anodic interfaces are identical in every cell, changes in the impedance spectra can be attributed to the different cathode catalysts, other interface and mass transport characteristics. Thus, it is reasonable to attribute the divergences in the amplitude responses at low current densities to varying charge transfer and interface resistances at the cathode. These resistances seem to be similar for the PGM catalysts and the Magnéli phase catalyst, whereas the resulting values for the carbon-based catalysts are higher. The lower the charge transfer resistance is, the faster is the kinetics of the respective reaction. In this case, the HER kinetics of the Pt/C, IrO_2 and the Magnéli phase catalyst are the fastest, followed by $[Mo_3S_{13}]^{2-}$@N-CNT. The HER kinetics on N-doped CNT are the slowest.

Figures 6b and 6d show the phase response of the impedance spectra at 100 mA cm^{-2} and 500 mA cm^{-2}, respectively. Usually, positive phase values are neglected during analysis of the impedance data because they are assumed to be caused by inductive effects of the measurement setup (e.g. cables). Therefore, the phase plots only show negative values. Herein, deviations between the catalysts and between the current densities can be observed. At 100 mA cm^{-2} (Fig. 6b), the phase response of all cell configurations, except when using N-doped CNT, are similar. For the PGM catalysts and the Magnéli phase catalyst, only one distinct minimum in the phase shift at approximately 20 Hz can be observed. For $[Mo_3S_{13}]^{2-}$@N-CNT the minimum at higher frequencies is more pronounced as for the other catalysts. In the phase response of N-doped CNT, there are also two overlapping minima which are shifted to higher frequencies and higher absolute phases compared to the other cell configurations. This is a result of the higher cathodic charge transfer resistance as seen in Fig. 6a and a lower capacitance compared to the other catalysts. A lower capacitance also explains the frequency shift of the intersection with the abscissa to higher frequency values.[45]

The phase responses at 500 mA cm^{-2} (Fig. 6d) generally show lower phase values than at the lower current density. This is a result of lower charge transfer resistances of the electrodes with increasing current density. The cell configurations with Pt/C, IrO_2 and the Magnéli phase catalyst again show a qualitatively similar phase response. In contrast to 100 mA cm^{-2}, another phase minimum at frequencies below 1 Hz is present. This might be attributed to

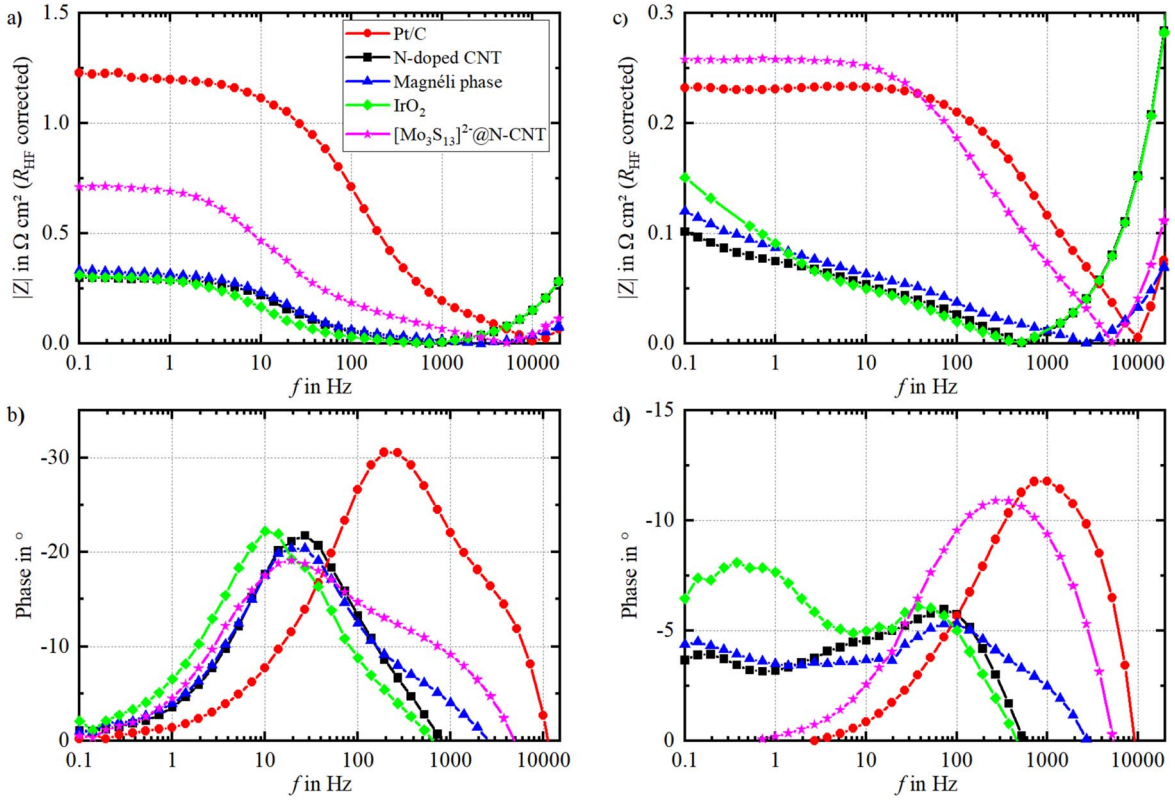

Figure 6. Presentation of the electrochemical impedance data in Bode plots. The R_{HF}-corrected amplitudes |Z| at 100 mA cm^{-2} and 500 mA cm^{-2} are shown in a) and c), respectively. The corresponding phase responses at 100 mA cm^{-2} are displayed in b) and at 500 mA cm^{-2} in d).

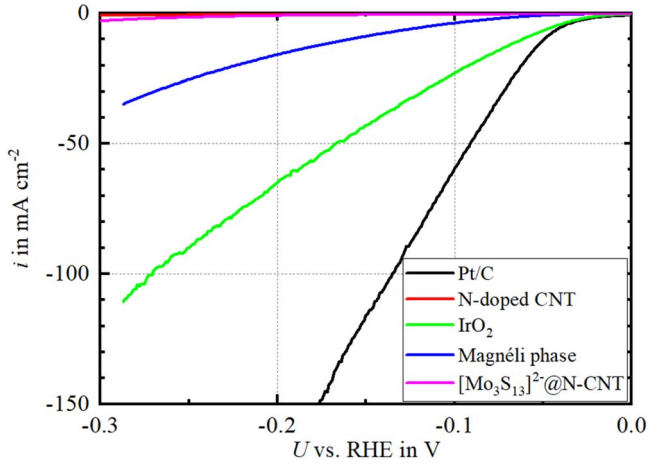

Figure 7. Catalyst-specific hydrogen evolution activity measured with linear sweep voltammetry in N_2-saturated sulfuric acid solution (0.5 M), a rotation speed of 1000 rpm and a sweep rate of 15 mV s^{-1}. The catalysts were collected from the PTEs after full cell experiments.

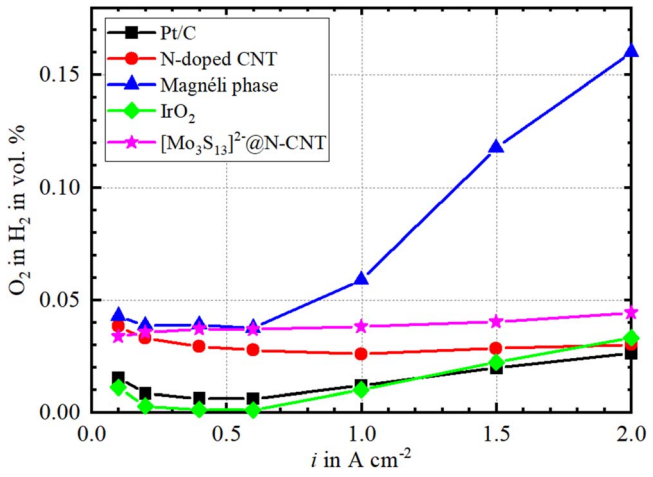

Figure 8. Measured oxygen in hydrogen volume fractions through Nafion 115 at 80 °C and ambient pressure.

changes of the mass transport, possibly caused by different electrode structures. As seen in the SEM images (Fig. 2), the surfaces of these three catalysts were noticeably smoother than of the carbon-based catalysts. The carbon-based catalysts show only one distinct phase minimum at higher frequencies with a higher absolute value. As seen in Fig. 6c), R_{CT} of $[Mo_3S_{13}]^{2-}$@N-CNT is higher than of N-doped CNT. Due to the deposition of the CNTs with $[Mo_3S_{13}]^{2-}$, the surface area of $[Mo_3S_{13}]^{2-}$@N-CNT is assumed to be higher than the surface area of the bare CNTs. As the capacitance correlates with the surface area, a higher capacitance follows for $[Mo_3S_{13}]^{2-}$@N-CNT. This results in a lower frequency for the phase minimum.

These findings could be proven by *ex situ* LSV in a RDE-setup (Fig. 7) in which the activity of the HER was measured. The observed trend in electrocatalytic activity for the HER is similar to the previously described data obtained from the Tafel plots in Fig. 5. Figure 7 clearly shows that Pt/C has the highest activity, followed by IrO_2 and the Magnéli phase. Although these three catalysts show different half-cell polarisations, they result in very similar polarisation behaviours in full cells (cf. Fig. 3 and Fig. 5). Apparently, the OER is still the limiting reaction when using these cathode catalysts. In contrast, the carbon-based electrocatalysts need high overpotentials to let the hydrogen evolution reaction occur (Fig. 7). In terms of the full cell polarisation behaviour (cf. Fig. 3), this results in a shift

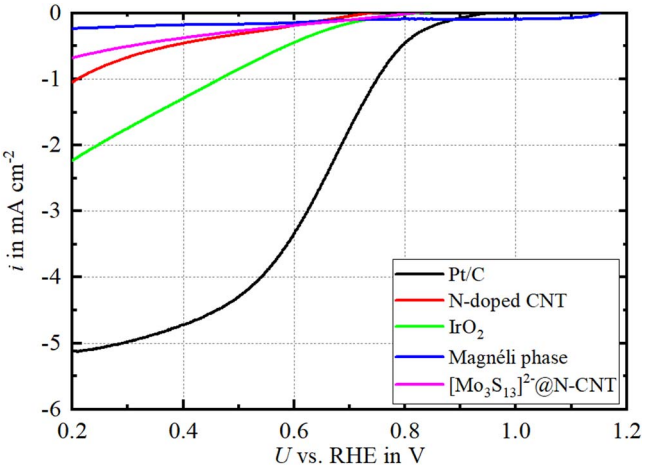

Figure 9. Catalyst-specific oxygen reduction activity measured by linear sweep voltammetry in O_2-saturated perchloric acid solution (0.1 M), a rotation speed of 1600 rpm and a sweep rate of 5 mV s^{-1}. The catalysts were collected from the PTEs after full cell experiments.

towards higher voltages. In contrast to the work of Holzapfel *et al.*,[32] the activity of $[Mo_3S_{13}]^{2-}$@N-CNT in this work is far lower. They assume that the catalyst passes a structural transformation at current densities higher than 2 A cm^{-2}, which leads to an enhanced electrochemical activity. Therefore, it can be possible that the catalyst in this work was not fully activated which would explain the low activity towards the HER. However, these findings can only give a theoretical indication, since the real performance is only visible in full cell experiments.

Oxygen crossover.—The measured oxygen content in the hydrogen product gas, which was determined by gas chromatography, is shown in Fig. 8. Generally, the cells with PGM cathode catalysts show lower oxygen in hydrogen contents than the PGM-free configurations. For the well performing cell configurations (Pt/C, IrO_2 and Magnéli phase) the oxygen in hydrogen content is increasing with increasing current density. The measured oxygen contents for the two carbon-based catalysts remains almost constant over the investigated current range.

The cells using the PGM catalysts (Pt/C and IrO_2) show the lowest oxygen content. Additionally, the lowest cell voltages were obtained with these catalysts (cf. Fig. 3). It was expected that the oxygen volume fraction using Pt/C is low, because platinum is a good catalyst for the recombination of hydrogen and oxygen to water. Consequently, the major part of permeated oxygen recombines with evolving hydrogen. Below 1 A cm^{-2}, the measured oxygen fraction using IrO_2 is lower than with Pt/C. An explanation could be the catalyst loading of IrO_2, which is three times higher than the loading of Pt/C. It can be assumed that the surface area and thus, the number of active recombination sites, is higher. This eventually leads to a lower oxygen in hydrogen fraction at low current densities.

The measured oxygen content using N-doped CNT is higher than with the PGM catalysts. They approach similar contents at 2 A cm^{-2}. Compared to the bare nanotubes, the values using $[Mo_3S_{13}]^{2-}$@N-CNT are shifted to slightly higher oxygen in hydrogen volume fractions. Up to approximately 0.6 A cm^{-2}, the cells with the Magnéli phase catalyst and $[Mo_3S_{13}]^{2-}$@N-CNT show similar oxygen contents. A further increase of the current density results in a significant increase of the oxygen content when using the Magnéli phase catalyst. At 2 A cm^{-2}, the measured oxygen content in hydrogen with this catalyst is more than the fivefold value of Pt/C. From these results the recombination properties of the catalysts can be estimated qualitatively. The Magnéli phase catalyst appears to have the lowest activity, whereas the PGM catalysts (Pt/C

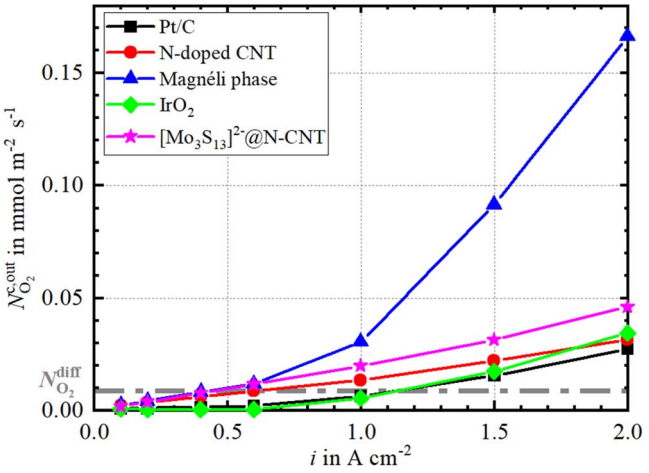

Figure 10. Cathodic oxygen flux through Nafion 115 at the cathode cell outlet using the different cathode electrocatalysts at 80 °C and ambient pressure.

and IrO_2) have a high recombination activity. The recombination activities of the two carbon-based catalysts should be somewhere in between.

This trend in recombination activity is supported by *ex situ* measurements, in which the ORR activity was determined by LSV (Fig. 9). The recombination of hydrogen and oxygen can occur via an electrochemical or a chemical pathway. In the used full cell setup, probably both pathways occur simultaneously. On electrically isolated particles, only the chemical pathway proceeds. We have tried to measure the chemical recombination rate by flushing the cathode side of the unpolarised cell with an O_2 in H_2 mixture of known concentration. Unfortunately, our setup was either not sensitive enough to measure changes in the gas composition or this approach was unable to mimic the experimental conditions in the cell during electrolysis.

As seen, the measurement of the pure chemical recombination rate is quite difficult and needs special experimental setups. Therefore, the activity for the oxygen reduction reaction of each catalyst will be used as a measure for their recombination activities.

According to Sabatier's principle, the interaction between a catalyst and the reactants should be neither too strong nor too weak. Platinum fulfils this requirement for hydrogen and oxygen. Consequently, it is the state of the art catalyst for hydrogen evolution, hydrogen oxidation and oxygen reduction.[4,49,50] Therefore, we assume that catalysts which show a high activity for the ORR also show high activities for the chemical recombination of hydrogen and oxygen.

The kinetics for the oxygen reduction reaction were determined similarly to the determination of the hydrogen evolution activity in the previous section (cf. Fig. 7). The results of the LSV measurements are displayed in Fig. 9. In general, the measured currents are significantly lower compared to the hydrogen evolution. This is caused by the complex, sluggish oxygen reduction kinetics which are accompanied by higher overpotentials. The state of the art cathode catalyst (Pt/C) shows the highest onset potential for the oxygen reduction reaction. IrO_2, N-doped CNT and $[Mo_3S_{13}]^{2-}$@N-CNT have a poorer activity for the ORR compared to platinum. The Magnéli phase catalyst shows almost no activity for the reaction, although a small amount of the mixed Ti-Ir phase exists alongside the pure Ti Magnéli phase. Thus, the electrocatalytic activity for the ORR according to the LSV measurements decreases in this order: Pt/C > IrO_2 > N-doped CNT > $[Mo_3S_{13}]^{2-}$@N-CNT > Magnéli phase. This qualitative trend in ORR activities fits well to the results in Fig. 8.

As already mentioned, the measured oxygen in hydrogen fraction using IrO_2 is lower than using Pt/C, although the ORR activity of Pt/C is higher. However, it has been reported elsewhere[4,51] that the activity of metallic Ir and IrO_2 regarding the oxygen reduction cannot compete with platinum. This explains the differences of the two PGM catalysts in Fig. 9 and at current densities above 1 A cm^{-2} in Fig. 8. Nonetheless, IrO_2 is a quite good HER catalyst as shown in the previous section. This is explained by a high affinity of the oxide surface to hydrogen, which is even higher compared to platinum.[24–26]

In contrast to the HER activity, the bare CNT catalyse the ORR better than the $[Mo_3S_{13}]^{2-}$@N-CNT. The role of doped carbon catalysts as a noble metal free alternative for the oxygen reduction reaction is of high interest in the field of PEM fuel cell research. In theirs review of using such catalysts in PEM fuel cells, Klingele *et al.*[52] and Liu *et al.*[53] explain the enhanced ORR activity of doped carbon materials with the polarisation of bonds. Introducing heteroatoms such as nitrogen into the graphitic structure results in a polarisation of the bonds neighbouring the dopant atom. It is assumed that the adsorption at such polarised carbon atoms facilitates oxygen adsorption, which leads to an enhanced ORR activity. As the application of the $[Mo_3S_{13}]^{2-}$–clusters onto the CNTs may block some of the active sites for oxygen adsorption, the decreased ORR activity in comparison to the bare CNTs can be explained. The catalytic activity of graphitic carbons for the recombination of hydrogen and oxygen is known in literature.[54,55]

Figure 10 shows the measured cathodic oxygen flux $N_{O_2}^{c,out}$ calculated from the data displayed in Fig. 8 according to Eq. 4. The measured oxygen fluxes increase with increasing current density. This phenomenon was measured and explained in previous works by Trinke *et al.* for both hydrogen and oxygen crossover.[5,19,23] The higher the aforementioned recombination activity of the used cathode catalyst is, the lower is the value of $N_{O_2}^{c,out}$. In a previous work, Trinke *et al.*[23] demonstrated the current dependency of oxygen crossover using Pt and a Pt-free cathode catalyst. The results show the same qualitative trend as in this work: The measured oxygen crossover flux with Pt-free catalysts is higher than with Pt.

Further, the diffusional oxygen flux $N_{O_2}^{diff}$ from anode and cathode, as defined in Eq. 5, is shown in Fig. 10(dashed line). As mentioned previously, the permeation of oxygen not only proceeds by diffusive transport but also by convection. However, the ratio of both transport mechanisms during water electrolysis operation cannot be distinguished, since both occur simultaneously and additionally, the amount of recombined oxygen in unknown. Therefore, $N_{O_2}^{diff}$ should be measured at minimum when no permeated oxygen recombines with hydrogen. However, this is not the case no matter which catalyst was used. Consequently, the difference between $N_{O_2}^{diff}$ and the actually measured oxygen flux corresponds to the minimum amount of recombined oxygen. The more active a cathode catalyst was determined for the recombination reaction, the longer the curve falls below this theoretical minimum value. For Pt/C and IrO_2, 1 A cm^{-2} needs to be exceeded in order to measure higher values than $N_{O_2}^{diff}$. Using the Magnéli phase as a catalyst, 0.4 A cm^{-2} suffices to cross the theoretical value. Although the Magnéli phase catalyst barely showed an activity for the oxygen reduction reaction (cf. Fig. 9), the remaining catalytic activity seems to be high enough to let the permeated oxygen recombine almost completely at low current densities.

Further reasons for the current dependency of measured oxygen crossover can be found in the rate law for the chemical recombination reaction. If a rate law according to Eq. 6 is assumed for the recombination, then the recombination rate r_{rec} can be influenced by the concentration of hydrogen c_{H_2} or by the concentration of oxygen

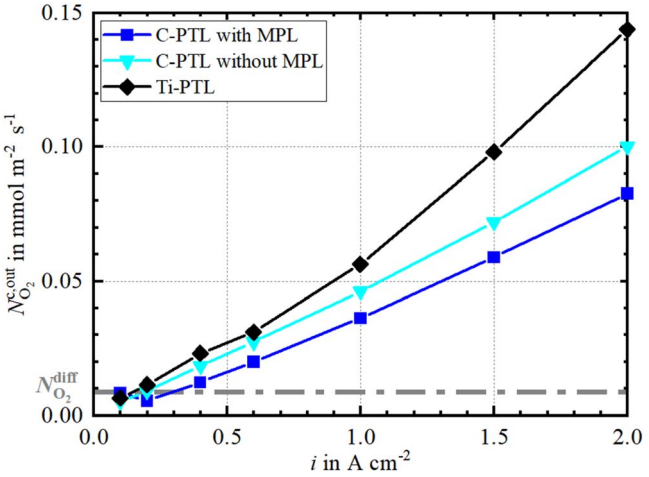

Figure 11. Cathodic oxygen flux through Nafion 115 using the Magnéli phase catalyst and different gas transport layers at the cathode at 80 °C and ambient pressure.

c_{O_2}. Both concentrations are influenced by the current density. As the concentration of hydrogen at the cathode can be assumed as overstoichiometrically high, the reaction rate solely depends on c_{O_2}.

$$r_{rec} = k_{rec} \cdot c_{H_2}^{x} \cdot c_{O_2}^{y} \quad [6]$$

The high hydrogen flux at high current densities leads to a shorter residence time of permeated oxygen in the cathodic compartment. Hence, the time for recombination is higher at lower current densities. Further, the increasing reaction rate for the hydrogen evolution with higher current densities leads to an occupation of more catalytically active sites. The recombination reaction is suppressed by the ongoing adsorption of hydrogen. From the electrochemical point of view, it can be possible that the cathodic potentials may differ when comparing the different catalysts, as the hydrogen evolutions kinetics differ as well. There might be a dependency of the recombination and the cathodic potential.

Up to this point, it can be concluded that both N-doped CNT and $[Mo_3S_{13}]^{2-}$@N-CNTs show far slower hydrogen evolution kinetics, but the recombination activities remain high enough to let permeated oxygen recombine with hydrogen. The Magnéli phase catalyst is the only PGM-free catalyst showing similar HER kinetics as Pt, while its recombination activity is the lowest of all investigated catalysts. In order to evaluate the amount of permeated oxygen from the anode to the cathode during electrolysis, a cathode catalyst with a low or no recombination activity has to be used. Up to this point, only the Magnéli phase catalyst seems to be a proper catalyst for measuring the oxygen crossover during electrolysis while maintaining a good cell polarisation. However, the real amount of permeated oxygen is probably far higher than the results indicate.

Recombination properties of carbon-based porous transport layers.—As seen in the previous section, the two carbon-based catalysts showed quite good recombination properties, as their onset potentials for the ORR (Fig. 9) was only slightly lower than of IrO_2 and Pt/C and the measurable oxygen crossover was lower than the minimum diffusional crossover through a Nafion membrane (Fig. 10). As CNTs consist of graphitic carbon and as the state of the art PTLs for the cathode usually are made out of conductive, graphitic carbon, we wondered if the PTL material itself also shows a measurable catalytic activity for the recombination of oxygen and hydrogen to water.

For this study, the Magnéli phase catalyst was applied on the uncoated side of the half-coated CCM to obtain a "normal" catalyst coated membrane. The catalyst was chosen as it showed the lowest activity for the recombination reaction. For the characterisation of the recombination properties of the PTL, the PTL material was varied: a carbon PTL with MPL (high surface area), the same PTL without MPL and a PTL made out of Ti-fibres. We assume that the titanium substrate will not catalyse the recombination reaction as the adsorption energy of hydrogen on titanium is too high.[4]

The measurement of oxygen in hydrogen content followed the same procedure as with the PTEs. The resulting oxygen fluxes at the cathode cell outlet are displayed in Fig. 11. In comparison to the measured oxygen flux with the Magnéli phase PTE in Fig. 10, the qualitative trend using the CCMs is rather linear with current density. The discrepancies between the PTE and CCM data is probably caused by different structures of the catalyst layer due to the manufacturing process.

As expected, the carbon-based PTLs show lower oxygen fluxes than the Ti-PTL and thus, we can assume that carbon-based PTLs have a noticeable catalytic activity for the recombination reaction. Moreover, it can be assumed that the higher the surface area of the PTL is, the more recombination sites exist. As the surface area of the PTL with MPL is higher than without the MPL, the lower oxygen flux when using the PTL with MPL can be explained. However, the diffusional oxygen flux at low current densities is again not reached. This is another indicator that the recombination properties of the used Magnéli phase catalyst are high enough to let the permeated oxygen recombine with hydrogen at low current densities.

Conclusions

In this work, two PGM and three PGM-free cathode catalysts for PEMWE were characterised regarding their electrochemical polarisation behaviour and their catalytic properties towards the hydrogen-oxygen recombination reaction. The investigated PGM catalysts (Pt/C and IrO_2) have shown the lowest cell voltages over the investigated current density range, whereas the usage of the two carbon-based PGM-free electrocatalysts (N-doped CNT and $[Mo_3S_{13}]^{2-}$@N-CNT) resulted in the highest cell voltages. Interestingly, the cell polarisation of the third PGM-free catalyst, namely Magnéli phase, was comparable to the PGM catalysts. The analysis of the cell voltage implied that the HER kinetics on the carbon-based catalyst have to be slower compared to the PGM catalysts. Further, the integral cell impedance spectra and *ex situ* LSV measurements for determining the HER activity prove the assumption of different HER kinetics.

The recombination properties of the five cathode catalysts were investigated by measuring the amount of permeated oxygen from the anode to the cathode by gas chromatography and by *ex situ* LSV measurements for determining the ORR activity. It was shown that catalysts with high ORR activities are better recombination catalysts as the measured oxygen in hydrogen content was lower than with using poor recombination catalysts. Using the Magnéli phase catalyst showed the highest oxygen in hydrogen fraction and concurrently the lowest ORR activity.

The relatively low measured oxygen contents when using the carbon-based catalysts raised the question if the commonly used carbon-based PTLs at the cathode also are catalytically active for the recombination of hydrogen and oxygen. For this additional study, CCMs with the Magnéli phase as cathodic catalyst were fabricated. The measured oxygen flux in the cathodic product gas showed lower fluxes with carbon PTLs than with a Ti-PTL. Further, it was shown that C-PTLs with larger surfaces (e.g. with MPL coating) exhibit more recombination sites than without a MPL.

However, the theoretical minimum oxygen flux caused by diffusion could not be reached in any configuration at current densities close to zero. This implies that even poor recombination catalysts, such as the Magnéli phase, are active enough to let an unknown amount of permeated oxygen recombine with hydrogen. The real amount of permeated oxygen is probably far higher than the results indicate. For a deeper understanding of the real oxygen crossover in PEM water electrolysis, an even more inactive catalyst

and an inactive PTL need to be used. Finding proper materials for this kind of study will be challenging.

In summary, it can be concluded that PGM-free cathode catalysts that can compete with the polarisation behaviour and HER kinetics of platinum, already exist. The recombination of permeated oxygen with evolving hydrogen will be reduced, which will lead to unpure hydrogen and inevitable processing of the product. However, the produced hydrogen gas is purified in the most cases anyway. Further, the long term stability of PGM-free catalysts needs to be assessed in future studies. An investigation of the mechanism of the recombination reaction on these catalysts is also of interest, as radical intermediates might be formed. The formation of reactive intermediates is undesirable, as they lead to a chemical degradation of the ionomer. Consequently, the possible advantage of the reduced radical formation needs to be investigated further in order to find alternative and cheap PGM-free cathode catalysts (e.g. Magnéli phase) to eventually replace platinum.

Acknowledgments

The authors gratefully acknowledge the financial support by the Federal Ministry of Education and Research of Germany in the framework of PowerMEE (BMBF /03SF0536).

ORCID

Agate Martin https://orcid.org/0000-0003-4673-1135
Patrick Trinke https://orcid.org/0000-0002-0935-532
Chuyen Van Pham https://orcid.org/0000-0002-0284-8430
Melanie Bühler https://orcid.org/0000-0002-8764-4428
Markus Bierling https://orcid.org/0000-0002-4992-2095
Boris Bensmann https://orcid.org/0000-0001-8685-7192
Simon Thiele https://orcid.org/0000-0002-4248-2752
Richard Hanke-Rauschenbach https://orcid.org/0000-0002-1958-307X

References

1. K. Ayers, N. Danilovic, R. Ouimet, M. Carmo, B. Pivovar, and M. Bornstein, *Annu. Rev. Chem. Biomol. Eng.*, **10**, 219 (2019).
2. M. Carmo, D. L. Fritz, J. Mergel, and D. Stolten, *Int. J. Hydrog. Energy*, **38**, 4901 (2013).
3. O. T. Holton and J. W. Stevenson, *Platin Met. Rev.*, **57**, 259 (2013).
4. P. Quaino, F. Juarez, E. Santos, and W. Schmickler, *Beilstein J. Nanotechnol.*, **5**, 846 (2014).
5. P. Trinke, B. Bensmann, S. Reichstein, R. Hanke-Rauschenbach, and K. Sundmacher, *J. Electrochem. Soc.*, **163**, F3164 (2016).
6. C. V. Pham, A. Zana, M. Arenz, and S. Thiele, *ChemElectroChem*, **5**, 2672 (2018).
7. J. Deng, P. Ren, D. Deng, L. Yu, F. Yang, and X. Bao, *Energy Environ. Sci.*, **7**, 1919 (2014).
8. B. Hinnemann, P. G. Moses, J. Bonde, K. P. Jørgensen, J. H. Nielsen, S. Horch, I. Chorkendorff, and J. K. Nørskov, *J. Am. Chem. Soc.*, **127**, 5308 (2005).
9. A. B. Laursen, S. Kegnæs, S. Dahl, and I. Chorkendorff, *Energy Environ. Sci.*, **5**, 5577 (2012).
10. Q. Feng, X. Yuan, G. Liu, B. Wei, Z. Zhang, H. Li, and H. Wang, *J. Power Sources*, **366**, 33 (2017).
11. T. Jahnke et al., *J. Power Sources*, **304**, 207 (2016).
12. T. Sugawara, N. Kawashima, and T. N. Murakami, *J. Power Sources*, **196**, 2615 (2011).
13. A. Laconti, H. Liu, C. Mittelsteadt, and R. McDonald, *ECS Trans.*, **1**, 199 (2006).
14. V. Schröder, B. Emonts, H. Janßen, and H.-P. Schulze, *Chem. Eng. Technol.*, **27**, 847 (2004).
15. M. Zatoń, J. Rozière, and D. J. Jones, *Sustain, Energ. Fuels*, **1**, 409 (2017).
16. M. Chandesris, V. Médeau, N. Guillet, S. Chelghoum, D. Thoby, and F. Fouda-Onana, *Int. J. Hydrogen Energy*, **40**, 1353 (2015).
17. F. Fouda-Onana, M. Chandesris, V. Médeau, S. Chelghoum, D. Thoby, and N. Guillet, *Int. J. Hydrogen Energy*, **41**, 16627 (2016).
18. S. A. Grigoriev, K. A. Dzhus, D. G. Bessarabov, and P. Millet, *Int. J. Hydrogen Energy*, **39**, 20440 (2014).
19. P. Trinke, P. Haug, J. Brauns, B. Bensmann, R. Hanke-Rauschenbach, and T. Turek, *J. Electrochem. Soc.*, **165**, F502 (2018).
20. P. Trinke, G. P. Keeley, M. Carmo, B. Bensmann, and R. Hanke-Rauschenbach, *J. Electrochem. Soc.*, **166**, F465 (2019).
21. H. Ito, N. Miyazaki, M. Ishida, and A. Nakano, *Int. J. Hydrog. Energy*, **41**, 20439 (2016).
22. M. Schalenbach, T. Hoefner, P. Paciok, M. Carmo, W. Lueke, and D. Stolten, *J. Phys. Chem. C*, **119**, 25145 (2015).
23. P. Trinke, B. Bensmann, and R. Hanke-Rauschenbach, *Electrochem. Commun.*, **82**, 98 (2017).
24. C. Chabanier and D. Guay, *J. Electroanal. Chem.*, **570**, 13 (2004).
25. Y. Cho, A. Yu, C. Lee, M. H. Kim, and Y. Lee, *ACS Appl. Mater. Interfaces*, **10**, 541 (2018).
26. M. Blouin and D. Guay, *J. Electrochem. Soc.*, **144**, 573 (1997).
27. T. Röpke and S. Möller, *Katalysatoren für die elektrochemische Wasserstoffentwicklung* (DE 10 2009 002 326 A1 2010.10.14) (2010), https://patentimages.storage.googleapis.com/ae/63/e4/e0a7e26d824035/DE102009002326A1.pdf.
28. J. Zeng, Z. Chen, X. Zhao, W. Yu, S. Wu, J. Lu, K. P. Loh, and J. Wu, *ACS Appl. Nano Mater.*, **2**, 7969 (2019).
29. J. Ekspong, T. Sharifi, A. Shchukarev, A. Klechikov, T. Wågberg, and E. Gracia-Espino, *Adv. Funct. Mater.*, **26**, 6766 (2016).
30. T. F. Jaramillo, K. P. Jorgensen, J. Bonde, J. H. Nielsen, S. Horch, and I. Chorkendorff,, *Science*, **317** (2007).
31. K. Zhang, Y. Zhao, S. Zhang, H. Yu, Y. Chen, P. Gao, and C. Zhu, *J. Mater. Chem. A*, **2**, 18715 (2014).
32. P. Holzapfel, M. Bühler, D. Escalera-López, M. Bierling, F. Speck, K. Mayrhofer, S. Cherevko, C. V. Pham, and S. Thiele, *Small*, **16**, 2003161 (2020).
33. M. Bühler, F. Hegge, P. Holzapfel, M. Bierling, M. Suermann, S. Vierrath, and S. Thiele, *J. Mater. Chem. A*, **7**, 26984 (2019).
34. C. Klose, P. Trinke, T. Böhm, B. Bensmann, S. Vierrath, R. Hanke-Rauschenbach, and S. Thiele, *J. Electrochem. Soc.*, **165**, F1271 (2018).
35. S. A. Grigoriev, A. A. Kalinnikov, P. Millet, V. I. Porembsky, and V. N. Fateev, *J. Appl. Electrochem.*, **40**, 921 (2010).
36. H. Ito, T. Maeda, A. Nakano, and H. Takenaka, *Int. J. Hydrog. Energy*, **36**, 10527 (2011).
37. L. Haar, J. S. Gallagher, and G. S. Kell, *NBS/NRC Steam Tables* (Hemisphere Publ. Corporation, Washington) (1984).
38. T. Schuler, T. J. Schmidt, and F. N. Büchi, *J. Electrochem. Soc.*, **166**, F555 (2019).
39. F. Hegge, R. Moroni, P. Trinke, B. Bensmann, R. Hanke-Rauschenbach, S. Thiele, and S. Vierrath, *J. Power Sources*, **393**, 62 (2018).
40. C.-H. Lin, *Appl. Energy*, **104**, 898 (2013).
41. S. H. Frensch, A. C. Olesen, S. S. Araya, and S. K. Kær, *Electrochim. Acta*, **263**, 228 (2018).
42. M. Suermann, T. J. Schmidt, and F. N. Büchi, *Electrochim. Acta*, **211**, 989 (2016).
43. E. Barsoukov and J. R. Macdonald, *Impedance Spectroscopy: Theory, Experiment, and Applications* (Wiley, Hoboken NJ) (2018).
44. P. Chulkin and P. Data, *J. Vis. Exp.*, **140**, e56611 (2018).
45. M. R. Schuster, *Mechanistische Untersuchung und Modellierung der Anodenreaktion in der Karbonat-Brennstoffzelle* (University of Ulm, Ulm, Germany) (2010).
46. C. Rozain and P. Millet, *Electrochim. Acta*, **131**, 160 (2014).
47. S. Siracusano, N. van Dijk, E. Payne-Johnson, V. Baglio, and A. S. Aricò, *Appl. Catal. B*, **164**, 488 (2015).
48. S. Siracusano, S. Trocino, N. Briguglio, V. Baglio, and A. S. Aricò, *Materials (Basel, Switzerland)*, **11**, 1368 (2018).
49. A. Kulkarni, S. Siahrostami, A. Patel, and J. K. Nørskov, *Chem. Rev.*, **118**, 2302 (2018).
50. Z. W. Seh, J. Kibsgaard, C. F. Dickens, I. Chorkendorff, J. K. Nørskov, and T. F. Jaramillo, *Science (New York, N.Y.)*, **355** (2017).
51. E. Antolini, *ACS Catal.*, **4**, 1426 (2014).
52. M. Klingele, C. V. Pham, A. Fischer, and S. Thiele, *Fuel Cells*, **16**, 522 (2016).
53. X. Liu and L. Dai, *Nat. Rev. Mater.*, **1**, 760 (2016).
54. H. Dietz, L. Dittmar, D. Ohms, M. Radwan, and K. Wiesener, *J. Power Sources*, **40**, 175 (1992).
55. K. Waki, R. A. Wong, H. S. Oktaviano, T. Fujio, T. Nagai, K. Kimoto, and K. Yamada, *Energy Environ. Sci.*, **7**, 1950 (2014).